On the relationship between azimuthal anisotropy from shear wave splitting and surface wave tomography

T. W. Becker,[1] S. Lebedev,[2] and M. D. Long[3]

[1]   Seismic anisotropy provides essential constraints on mantle dynamics and continental evolution. One particular question concerns the depth distribution and coherence of azimuthal anisotropy, which is key for understanding force transmission between the lithosphere and asthenosphere. Here, we reevaluate the degree of coherence between the predicted shear wave splitting derived from tomographic models of azimuthal anisotropy and that from actual observations of splitting. Significant differences between the two types of models have been reported, and such discrepancies may be due to differences in averaging properties or due to approximations used in previous comparisons. We find that elaborate, full waveform methods to estimate splitting from tomography yield generally similar results to the more common, simplified approaches. This validates previous comparisons and structural inversions. However, full waveform methods may be required for regional studies, and they allow exploiting the back-azimuthal variations in splitting that are expected for depth-variable anisotropy. Applying our analysis to a global set of *SKS* splitting measurements and two recent surface wave models of upper-mantle azimuthal anisotropy, we show that the measures of anisotropy inferred from the two types of data are in substantial agreement. Provided that the splitting data is spatially averaged (so as to bring it to the scale of long-wavelength tomographic models and reduce spatial aliasing), observed and tomography-predicted delay times are significantly correlated, and global angular misfits between predicted and actual splits are relatively low. Regional anisotropy complexity notwithstanding, our findings imply that splitting and tomography yield a consistent signal that can be used for geodynamic interpretation.

Citation: Becker, T. W., S. Lebedev, and M. D. Long (2012), On the relationship between azimuthal anisotropy from shear wave splitting and surface wave tomography, *J. Geophys. Res.*, *117*, B01306, doi:10.1029/2011JB008705.

1.   Introduction

[2]   Earth's structure and tectonic evolution are intrinsically linked by seismic anisotropy in the upper mantle and lithosphere, where convective motions are recorded during the formation of lattice-preferred orientation (LPO) fabrics under dislocation creep [e.g., *Nicolas and Christensen*, 1987; *Silver*, 1996; *Long and Becker*, 2010]. However, within the continental lithosphere, seismically mapped anisotropy appears complex [e.g., *Fouch and Rondenay*, 2006]. Transitions between geologically recent deformation and frozen-in anisotropy from older tectonic motions are reflected in layering [e.g., *Plomerova et al.*, 2002; *Yuan and Romanowicz*, 2010] and the stochastic character of azimuthal anisotropy in geological domains of different age [*Becker et al.*, 2007a,

2007b; *Wüstefeld et al.*, 2009]. Regional studies indicate intriguing variations of azimuthal anisotropy with depth, which may reflect decoupling of deformation or successive deformation episodes recorded at different depths [e.g., *Savage and Silver*, 1993; *Pedersen et al.*, 2006; *Marone and Romanowicz*, 2007; *Deschamps et al.*, 2008a; *Lin et al.*, 2011; *Endrun et al.*, 2011]. All of these observations hold the promise of yielding a better understanding of the long-term behavior of a rheologically complex lithosphere, including changes in plate motions and the formation of the continents.

[3]   Ideally, one would like to have a complete, three-dimensional (3-D) model of the full (21 independent components) elasticity tensor for such structural seismology studies. Fully anisotropic inversions are feasible, in principle [cf. *Montagner and Nataf*, 1988; *Panning and Nolet*, 2008; *Chevrot and Monteiller*, 2009], particularly if mineral physics and petrological information are used to reduce the dimensionality of the model parameter space [*Montagner and Anderson*, 1989; *Becker et al.*, 2006a]. However, often the sparsity of data requires, or simplicity and convenience demand, restricting the analysis to joint models that constrain only aspects of seismic anisotropy, for example the azimuthal kind, on which we focus here.

[1]Department of Earth Sciences, University of Southern California, Los Angeles, California, USA.
[2]Dublin Institute for Advanced Study, Dublin, Ireland.
[3]Department of Geology and Geophysics, Yale University, New Haven, Connecticut, USA.
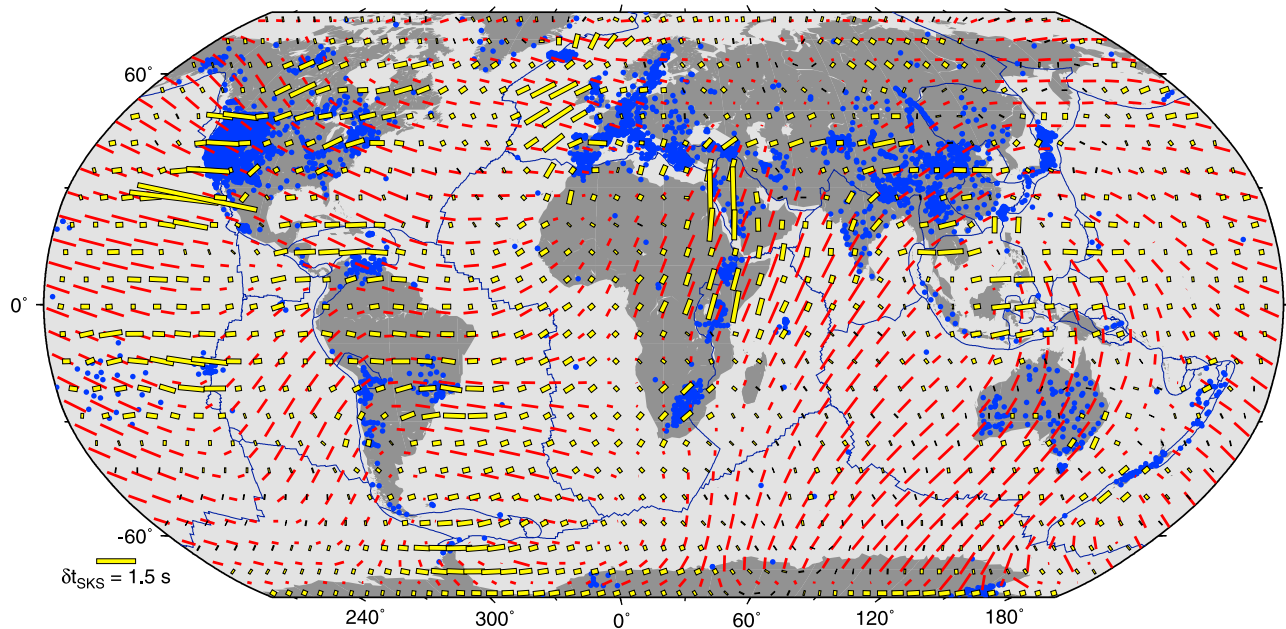
Figure 1. Distribution of *SKS* splitting in our merged database (blue dots, with 5159 station-averaged entries) and damped, $L = 20$, generalized spherical harmonics representation of *SKS* splitting (yellow sticks, see Appendix A), shown on top of the 200 km depth 2Ψ azimuthal anisotropy from *Lebedev and van der Hilst* [2008] (red sticks, equation (3)). Splitting measurements are mainly based on compilations by *Silver* [1996], *Fouch* [2003], and *Wüstefeld et al.* [2009], with additional references and data available at http://geodynamics.usc.edu/~becker/. Plate boundaries here and subsequently are from *Bird* [2003].

[4] For azimuthal anisotropy, hexagonal crystal symmetry is assumed with symmetry axis in the horizontal plane yielding a fast, v_{SV1}, and a slow, v_{SV2}, propagation direction for vertically polarized shear waves. Surface (Rayleigh) wave observations can constrain the anisotropic velocity anomaly, $G/L = (v_{SV1} - v_{SV2})/v_{SV}$, and the fast, Ψ, orientation for shear wave propagation. Here, G and L are the relevant elastic constants and v_{SV} the mean velocity, as defined by *Montagner et al.* [2000]. Given the dispersive nature of surface waves, phase velocity observations from different periods can be used to construct 3-D tomographic models for G/L and Ψ. Particularly in regions of poor coverage, tomographic models can be affected by the tradeoff between isotropic and anisotropic heterogeneity [e.g., *Tanimoto and Anderson*, 1985; *Laske and Masters*, 1998], which typically limits the lateral resolution to many hundreds of kilometers in global models [e.g., *Nataf et al.*, 1984; *Montagner and Tanimoto*, 1991; *Debayle et al.*, 2005; *Lebedev and van der Hilst*, 2008].

[5] This approach can then be contrasted with observations of shear wave splitting [e.g., *Ando et al.*, 1983; *Vinnik et al.*, 1984; *Silver and Chan*, 1988], typically from teleseismic *SKS* arrivals. A split shear wave is direct evidence for the existence of anisotropy. In its simplest form, a splitting measurement provides information on the azimuthal alignment of the symmetry axis, ϕ, of a single, hexagonally anisotropic layer and the delay time that the wave has accumulated between the arrival of the fast and the slow split S wave pulse, δt. With Fresnel-zone widths of $\sim$100 km, splitting measurements have relatively good lateral, but poor depth resolution, suggesting that body and surface wave

based anisotropy models provide complementary information (Figure 1).

[6] An initial global comparison between different azimuthal anisotropy representations was presented by *Montagner et al.* [2000] who compared the *SKS* splitting compilation of *Silver* [1996] with the predicted anisotropy, ϕ' and $\delta t'$, based on tomography by *Montagner and Tanimoto* [1991]. *Montagner et al.* [2000] found a poor global match with a bimodal coherence, $C(\alpha)$, as defined by *Griot et al.* [1998], which suggested typical angular deviations, α, between ϕ from *SKS* and ϕ' based on integration of Ψ and G/L from tomography of $\alpha \sim \pm 40°$, where $\alpha = \phi' - \phi$. An updated study was conducted by *Wüstefeld et al.* [2009], who used their own greatly expanded compilation of *SKS* splitting results and compared the coherence of azimuthal anisotropy with the predicted ϕ' obtained from the model of *Debayle et al.* [2005] on global and regional scales. *Wüstefeld et al.* [2009] conclude that the global correlation between the two representations of anisotropy was in fact "substantial." This improved match, with a more pleasing, single peak of C at zero lag, $\alpha = 0$, was attributed to improved surface wave model resolution and better global coverage by *SKS* studies. *Wüstefeld et al.* [2009] also explore a range of ways to represent ϕ from *SKS*. Their best global coherence values were, however, $C(0) \approx 0.2$, which is only $\sim$1.7 times the randomly expected coherence at equivalent spatial representation. While no correlation values were provided, a scatterplot of actual δt and $\delta t'$ from integration of G/L [*Wüstefeld et al.*, 2009, Figure 9] also shows little correlation of anisotropy strength.

[7] One concern with any studies that perform a joint interpretation of splitting and anisotropy tomography is that the shear wave splitting measurement does not represent

a simple average of the azimuthal anisotropy along the raypath [e.g., *Rümpker et al.*, 1999; *Saltzer et al.*, 2000; *Silver and Long*, 2011]. Typically, the method proposed by *Montagner et al.* [2000] for the case of small anisotropy and long period waves is used to compute predicted splitting from tomographic models [e.g., *Wüstefeld et al.*, 2009], and this basically represents a vectorial averaging, weighing all layers evenly along the ray path. In continental regions, fast orientations of azimuthal anisotropy and amplitudes may vary greatly with depth over the top ∼400 km of the upper mantle. We therefore expect significant deviations from simple averaging [*Saltzer et al.*, 2000] and, moreover, a dependence of both predicted delay time and fast azimuths of the splitting measurement on back-azimuth of the shear wave arrival [e.g., *Silver and Savage*, 1994; *Rümpker and Silver*, 1998; *Schulte-Pelkum and Blackman*, 2003]. It is therefore important to test the assumptions inherent in the *Montagner et al.* [2000] averaging approach, both to understand the global coherence between body and surface wave-based models of seismic anisotropy and to verify that regional, perhaps depth-dependent, deviations between the two are not partially an artifact of methodological simplifications.

[8] Here, we analyze two recent tomographic models of global azimuthal anisotropy and show what kinds of variations in splitting measurements can be expected based on a more complete treatment of predicted shear wave splitting that incorporates appropriate depth-integration. We show that, overall, the simplified predictions are suitable, but local variations between methods can be significant. We also reassess the match between predicted and actual splitting and show that smoother representations of Earth structure appear to match long-wavelength-averaged splitting quite well, albeit at much reduced amplitudes.

2. Splitting Estimation Methods

[9] Our goal is to estimate the predicted shear wave splitting from a tomographic model of seismic anisotropy in the Earth. In theory, this requires a 3-D representation of the full elasticity tensor along the raypath of whichever shear wave is considered, for *SKS* from the core mantle boundary to the surface. In practice, we focus on the uppermost mantle where most mantle anisotropy is concentrated [e.g., *Panning and Romanowicz*, 2006; *Kustowski et al.*, 2008], as expected given the formation of LPO under dislocation creep [*Karato*, 1992; *Becker et al.*, 2008; *Behn et al.*, 2009]. We will also not consider lateral variations of anisotropy on scales smaller than the Fresnel zone. This would require fully three-dimensional wave propagation methods [e.g., *Chevrot et al.*, 2004; *Levin et al.*, 2007] but is not warranted given the resolution afforded by tomographic models.

[10] The computation of shear wave splitting parameters from actual seismograms involves estimating the fast "axes" (i.e., the apparent fast polarization direction) and the delay time, and there are at least three ways of computing the equivalent, predicted ϕ' and $\delta t'$ parameters from tomography: *Montagner et al.* [2000] averaging of G/L azimuthal anomalies, computing splitting using the Christoffel matrix approach for an average tensor, and full waveform synthetic splitting.

2.1. Montagner Averaging of *G/L* Azimuthal Anomalies

[11] In the case of small anisotropy and long period waves (period $T > 10$ s), the predicted splitting for a tomographic model can be computed as [*Montagner et al.*, 2000]

$$\delta t' = \sqrt{f_c^2 + f_s^2} \quad \text{and} \quad \phi' = \frac{1}{2}\tan^{-1}\left(\frac{f_s}{f_c}\right), \tag{1}$$

where the vector components $f_{c,s}$ are the depth integrals (assuming a vertical path)

$$f_{c,s} = \int_0^a \sqrt{\frac{\rho}{L}}\frac{G_{c,s}}{L}dz = \int_0^a \frac{1}{v_{SV}}\frac{G_{c,s}}{L}dz, \tag{2}$$

a is the length of the path, $v_{SV} = \sqrt{L/\rho}$, ρ density, and c and s indices indicate the azimuthal cos and sin contributions to anisotropy, as follows: The relevant components of the elasticity tensor that determine the splitting are G/L with $G = \sqrt{G_c^2 + G_s^2}$, and the ratios $G_{c,s}/L$ relate to the typical parameterization of azimuthal-anisotropy tomography models

$$\frac{dv_{SV}}{v_{SV}} \approx A_0 + A_c \cos 2\Psi + A_s \sin 2\Psi \tag{3}$$

as

$$\frac{G_{c,s}}{L} = 2A_{c,s}. \tag{4}$$

Here, dv_{SV} is total the velocity anomaly with respect to a one-dimensional reference model, A_0 the isotropic velocity anomaly, and all higher order, 4Ψ, terms are neglected. Assuming vertical incidence and neglecting any effects due to isotropic anomalies A_0, the predicted splitting at every location can then be approximated by integration of the $A_{c,s}$ terms over depth, z, as in equation (2). To check if the assumptions of small anisotropy and long-period filtering might be violated on Earth and in actual *SKS* measurements and to estimate the degree of variability of ϕ' and $\delta t'$ with back-azimuth, we also compute splitting using two more elaborate methods.

2.2. Christoffel Matrix From Averaged Tensors

[12] We assume that the "real" anisotropic Earth can be approximated using the information in the azimuthally anisotropic surface wave models and convert the $A_{c,s}$ factors from tomography underneath each location into complete anisotropic tensors, C(z), as a function of depth. To obtain C(z), we tested several approaches, most simply aligning a best-fit, hexagonal approximation to an olivine-enstatite tensor in the horizontal plane, and then scaling the anisotropy such that the effective, transversely isotropic ("splitting") anomaly in the horizontal plane, δ_{TI}^h, corresponds to $2A_{c,s} = G/L$ from tomography at that depth (using the decomposition of *Browaeys and Chevrot* [2004]). We also consider an identically aligned, but fully anisotropic, depth-dependent olivine-enstatite tensor (as used in the work of *Becker et al.* [2006a]), again scaled such that $\delta_{TI}^h = 2A_{c,s}$, which adds orthorhombic symmetry components. Last, to explore the effect of dipping symmetry axes, we scaled down the full, hexagonally approximated olivine-enstatite tensor anisotropy by a factor of four to δ_{TI}^o and then aligned

the tensor at a dip angle of β out of the horizontal plane such that $\cos(\beta)\delta_{TI}^o = \delta_{TI}^h = 2A_{c,s}$ matched the azimuthal anisotropy from tomography, rescaling in an iterative step, if needed. The latter two approaches (nonhexagonal or dipping symmetry) are expected to yield a more complex splitting signal with back-azimuthal variations [e.g., *Schulte-Pelkum and Blackman*, 2003; *Browaeys and Chevrot*, 2004].

[13] From this anisotropic model where, for each location under consideration, we have estimates of $C(z)$ at each layer, we first compute a depth-averaged tensor $\tilde{C}$, using arithmetic, i.e., Voigt, averaging. From this average tensor, we then compute splitting as a function of incidence and back-azimuth based on the Christoffel equation [e.g., *Babuska and Cara*, 1991] using the implementation of *Schulte-Pelkum and Blackman* [2003]. Differently from the *Montagner et al.* [2000] averaging, this method not only yields ϕ' and $\delta t'$ but also simplified estimates of the variations of both parameters as a function of back-azimuth, σ_ϕ and $\sigma_{\delta t}$. When computing back-azimuthal variations, we fix the incidence angle to 5°, as a typical value for *SKS*. When averaging $C(z)$ for the Christoffel approach, we use constant weights for each layer, even though we expect surface-near regions to contribute more strongly in reality [e.g., *Rümpker et al.*, 1999; *Saltzer et al.*, 2000], because such wave propagation effects can be captured more fully by the method that is discussed next.

2.3. Full Waveform Synthetic Splitting

[14] Last, we also follow the approach suggested by *Hall et al.* [2000] to obtain splitting from geodynamic predictions of anisotropy, accounting for the full waveform complexities given the depth-dependent $C(z)$ model we can construct at each location using the method described above. Following *Becker et al.* [2006b], we first use a layer matrix computation that accounts for the depth dependence of anisotropy by assigning a constant tensor for each layer that the ray path crosses. This method assumes that lateral variations in material properties are small on the wavelengths of a Fresnel zone. Our waveform modeling approach is based on *Kennett* [1983], with extensions by *Booth and Crampin* [1985] and *Chapman and Shearer* [1989], and yields a pulse train. This is then bandpass-filtered to construct synthetic seismograms in *SKS*-typical bands of $T \approx 7$ s center period. We use mainly the cross-correlation method [e.g., *Fukao*, 1984; *Bowman and Ando*, 1987], implemented following *Levin et al.* [1999], to automatically measure splitting from modeled waveforms, scanning through the full back-azimuth of the incoming *SKS* waves. We discard nulls and poor measurements and report both the mean ("best") and standard deviations (σ_ϕ and $\sigma_{\delta t}$) of the inferred $\delta t'$ and ϕ' (for details, see *Becker et al.* [2006b]).

[15] The cross-correlation method is equivalent to the transverse-component minimization method [*Silver and Chan*, 1988] for a single horizontal layer in the absence of noise. However, cross-correlation should perform better in the case of multiple layers of anisotropy [*Levin et al.*, 1999; *Long and van der Hilst*, 2005] as is the case for some locales where Ψ rotates quite widely with depth (Figure 2). While detailed results of the splitting measurement depend on analysis choices such as filtering, windowing, and measurement method, general results are usually consistent [e.g.,

Long and van der Hilst, 2005; *Wüstefeld and Bokelmann*, 2007]. However, to test this assumption in the framework of our automated splitting setup, we also present some cases where splits were computed using the cross-convolution routine ah_cross_conv_1 of *Menke and Levin* [2003], which has a slightly different optimization strategy from our implementation of *Levin et al.* [1999] (all software and data used here are provided at http://geodynamics.usc.edu/~becker/). More importantly, we also experiment with the waveform filtering, allowing for longer periods of $T \approx 12.5$ s and $T \approx 15$ s to test how the approximation of *Montagner et al.* [2000] is affected.

3. Azimuthal Anisotropy Observations and Models

3.1. Shear Wave Splitting Database

[16] We maintain our own compilation of shear wave splitting measurements, mainly based on the efforts by *Silver* [1996] and *Fouch* [2003] but subsequently updated by addition of regional studies and now holding 9635 entries. For this study, our database was merged with that of *Wüstefeld et al.* [2009] which had 4778 entries as of May 2011, yielding a total of 14,326 splits. Our compilation includes measurements carried out by many different authors, and individual studies differ in the measurement methods used, processing choices such as event selection, filtering, windowing, and back-azimuthal coverage. Given such methodological concerns and the possibly large back-azimuth variation of splitting parameters if anisotropy is complex underneath a single station, it would be desirable to have a consistent measurement and waveform filtering strategy, and to take into account back-azimuth information. However, we only have event and method information for a small subset of the splits, which is why we discard this information subsequently. If we station-average the splits (using an arithmetic, vectorial mean of all nonnull splits, taking the 180° periodicity of ϕ into account), we are left with 5159 mean splitting values on which we base our analysis (Figure 1). Such averaging is expected to also reduce the effect of some of the inconsistencies of the splitting database, for example the mix between already station-averaged and individual splits reported. (An electronic version of this *SKS* compilation can be found at http://geodynamics.usc.edu/~becker/.)

[17] We will consider both this complete station-averaged data set and spatially averaged versions of it. Several averaging and interpolation approaches for shear wave splitting data have been discussed [e.g., *Wüstefeld et al.*, 2009]. Here, we use one global basis-function approach and a simple averaging scheme that does not make any assumptions about the statistical properties of the data. For a global, smoothed representation we use generalized spherical harmonics as implemented by *Boschi and Woodhouse* [2006]. For consistency with the tomographic models (see below), we use a maximum degree $L = 20$ (individual degree $\ell \in [2; L]$ for a 2Ψ type of signal) and perform a least-squares fit to the station-averaged splits (Appendix A). Such global representations assume that the field represented by the splits is smooth (which is not, but it may be seen as such by the tomographic models) and will extrapolate into regions without data.
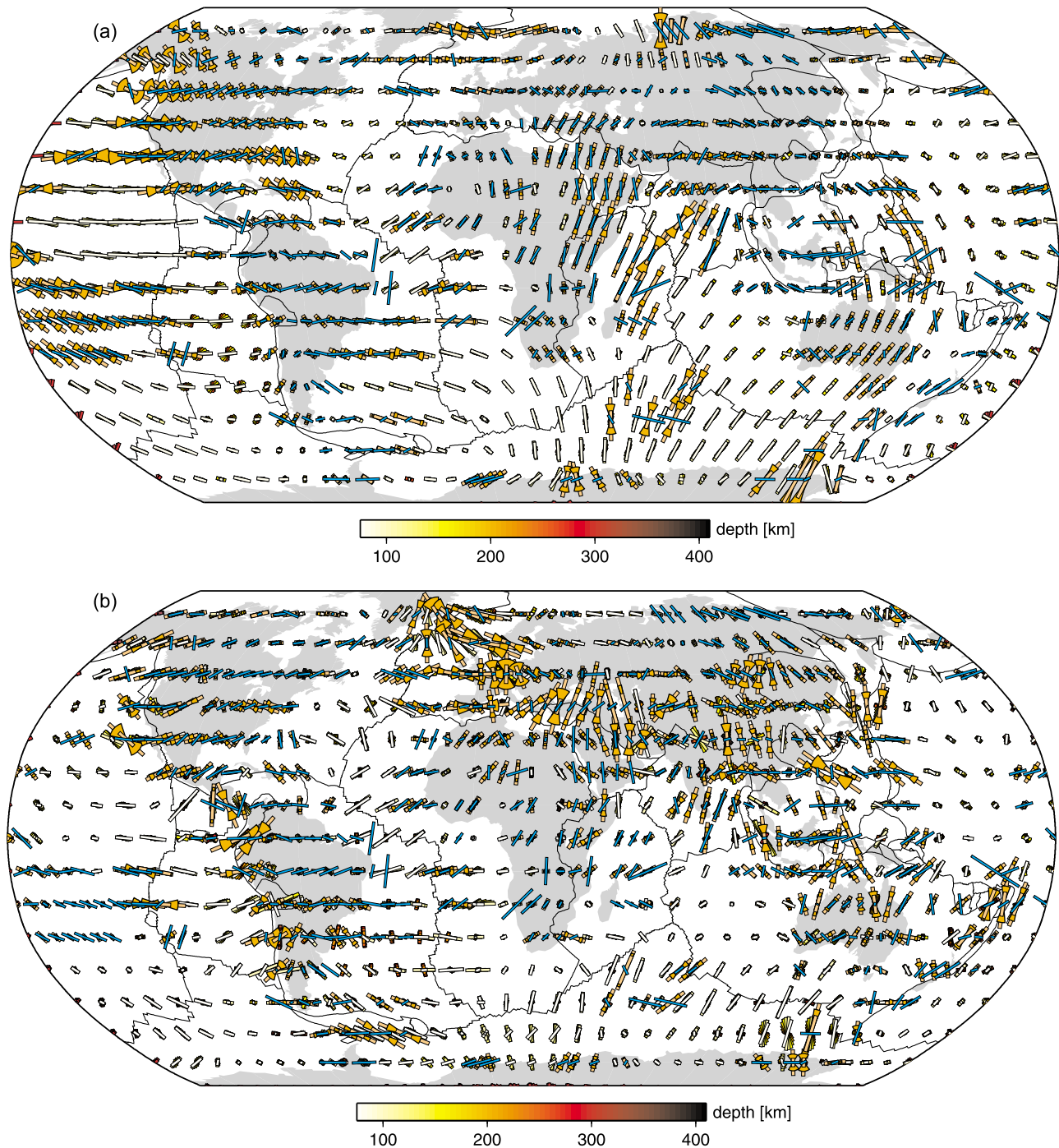
**Figure 2.** (a) Depth variation (75–410 km shown) of 2Ψ fast propagation direction in tomography model LH08 (sticks in background, see color bar for depth), splitting predicted from tomography with the full waveform method (orange, with larger and smaller sticks and wedge sizes indicating back-azimuthal variability for $\delta t' \pm \sigma_{\delta t}$ and $\phi' \pm \sigma_\phi$, respectively) and vectorial average of the measured splitting parameters (cyan) in the 5°-binned representation (cf. Figure 1). (b) Same for DKP2005. Stick length is adjusted for each model to account for amplitude variations between 2Ψ, $\delta t'$, and δt (cf. Figures 5 and 7).

[18] We therefore also use a simple, bin-averaged representation of γ resolution (say, $\gamma = 5°$). We compute the mean δt and ϕ for all data within γ distance from the binning sites which are spaced γ in latitude, λ, ($\lambda \in (-\pi, \pi)$) and with $\gamma/\cos(\lambda)$ in longitude. The results of the damped, spherical harmonics representation and the bin-averaged splitting are

generally consistent in areas of good data coverage (compare Figures 1 and 2).

[19] The regional characteristics of splitting have been discussed, for example, by *Vinnik et al.* [1992], *Silver* [1996], and *Wüstefeld et al.* [2009], so we will not go into much detail. However, we note that even updated *SKS*
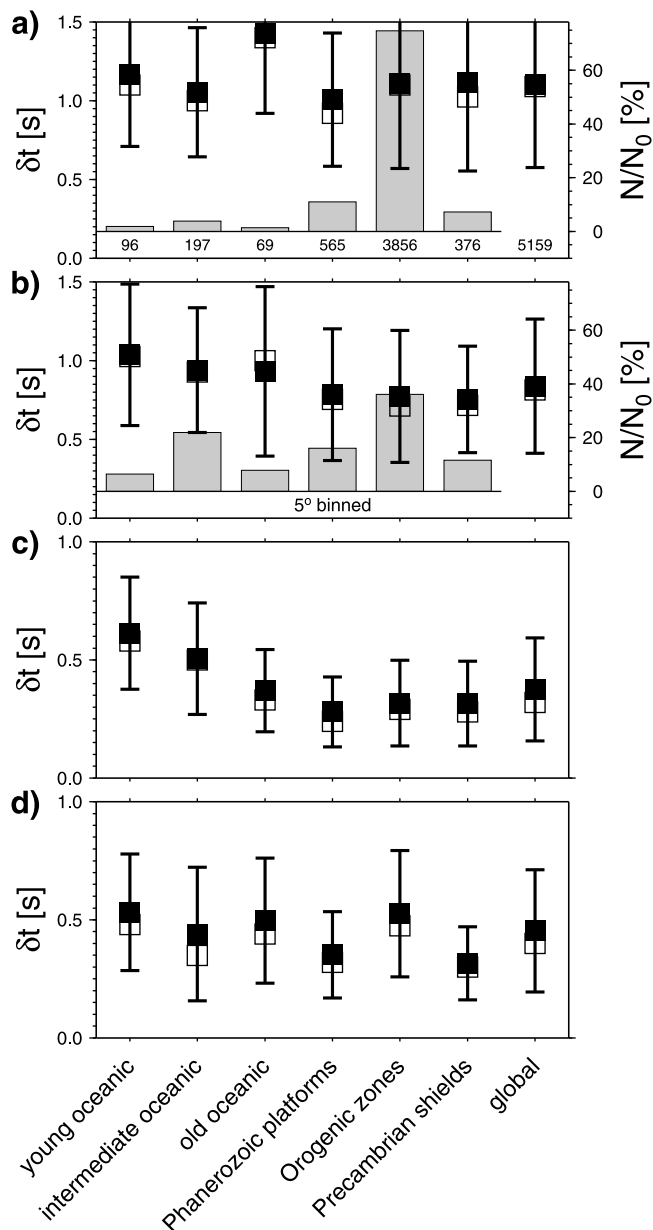
Figure 3. (a) Mean (filled boxes), standard deviation (error bars), and median (open boxes) of delay times, δt, in our station-averaged splitting database (Figure 1), sorted into GTR-1 [*Jordan*, 1981] tectonic regions. Orogenic zones are expected to be more geologically active than platforms, and shields are expected to be most stable and have the thickest lithosphere [cf. *Becker et al.*, 2007a]. Number, N, of data for each region are listed underneath gray bars, which indicate the relative frequency, N/N_0. (b) Same as Figure 3a but for a 5°-binned representation of the splitting data. (c) Predicted splitting computed with the full waveform method for the depth regions 75–410 km in tomography model LH08 (see text), evaluated at the 5°-binned sites of Figure 3b. (d) Same as Figure 3c but predicted splitting for DKP2005. (Note different δt scale for Figures 3c and 3d).

compilations remain strongly biased toward continental, and particularly tectonically active, regions such as the western United States (Figures 1 and 3). Figure 3a shows how the

data and delay times are distributed in terms of the GTR-1 tectonic regionalization [*Jordan*, 1981]. The regional bias is seen in the prominence of the orogenic zones (~75% of the data), which include regions such as the western United States, and hence also dominate the global statistics.

[20] If we partially correct for the data bias and consider the 5° averaged splitting (Figure 3b), there is almost no difference in the mean delay times within continental regions ($\langle \delta t \rangle_{\text{cont}} \approx 0.77$ s), but some indication of larger splitting underneath oceanic basins ($\langle \delta t \rangle_{\text{ocean}} \approx 0.96$ s), compared to the global mean $\langle \delta t \rangle \approx 0.84$ s. Even though δt distributions are typically (and necessarily) positively skewed, differences between median and mean are relatively small (Figures 3a and 3b; see also Figure 7a). Assuming normal distributions and independent sample values, the finding of larger $\langle \delta t \rangle$ in oceans compared to continents for Figures 3a and 3b can then be inferred to be more than 97.5% and 99.9% significant, respectively, using Welch's t-test.

3.2. Comparison of Tomographic Models

[21] We contrast the *SKS* splits with the two most recent, global azimuthal anisotropy models available to us, DKP2005 by *Debayle et al.* [2005] and LH08 by *Lebedev and van der Hilst* [2008], from both of which we use only the 2Ψ terms (Figure 2). Both models use fundamental mode Rayleigh waves and overtones to constrain upper mantle SV structure, but their datasets, theoretical assumptions, and inversion choices, such as on regularization and parameterization, are quite different and have been discussed elsewhere [*Debayle et al.*, 2005; *Becker et al.*, 2007b; *Lebedev and van der Hilst*, 2008]. We here simply treat them as two alternative representations of the "true," 3-D anisotropic structure of the Earth, realizing that tomography represents regionally variably resolved, smoothed approximations of the actual structure. For quantitative comparison purposes, we express both models in generalized spherical harmonics [see *Becker et al.*, 2007b], and Figures 4a and 4b show heterogeneity spectra at three layers in the upper mantle.

[22] The anisotropic heterogeneity amplitude decreases strongly from 50 to 350 km depth for both models. However, DKP2005 shows a much flatter decrease in power per spherical harmonic degree, ℓ, than LH08, meaning that the azimuthal anisotropy structure is more heterogeneous, even at the relatively smaller, regional scales. Such differences in the power spectra of tomography are expected given different inversion choices, but they are more pronounced for anisotropic than for isotropic models given the required additional choices as to how to regularize the inversions [*Becker et al.*, 2007b]. DKP2005's power continues to decrease roughly monotonically, as in Figure 4b, down to 10^{-4} at $\ell \sim 30$, but we will focus on relatively long-wavelength, maximum degree $L = 20$ because LH08 has little meaningful power beyond that point. Figure 4c shows the linear correlation per degree between DKP2005 and LH08 azimuthal anisotropy (taking both azimuth and amplitude of 2Ψ anomalies into account); it is statistically significant at the 95% level for most ℓ, but only above ~200 km depth.

[23] Figure 5 shows how the tomographic models represent azimuthal anisotropy with depth; both display a concentration of anisotropy at ~100 km (note range of depths where both models are defined in Figure 5a), with DKP2005 having larger amplitudes of up to an RMS, $(v_{SV1} - v_{SV2})/v_{SV}$,

a) LH08

b) DKP2005

c)
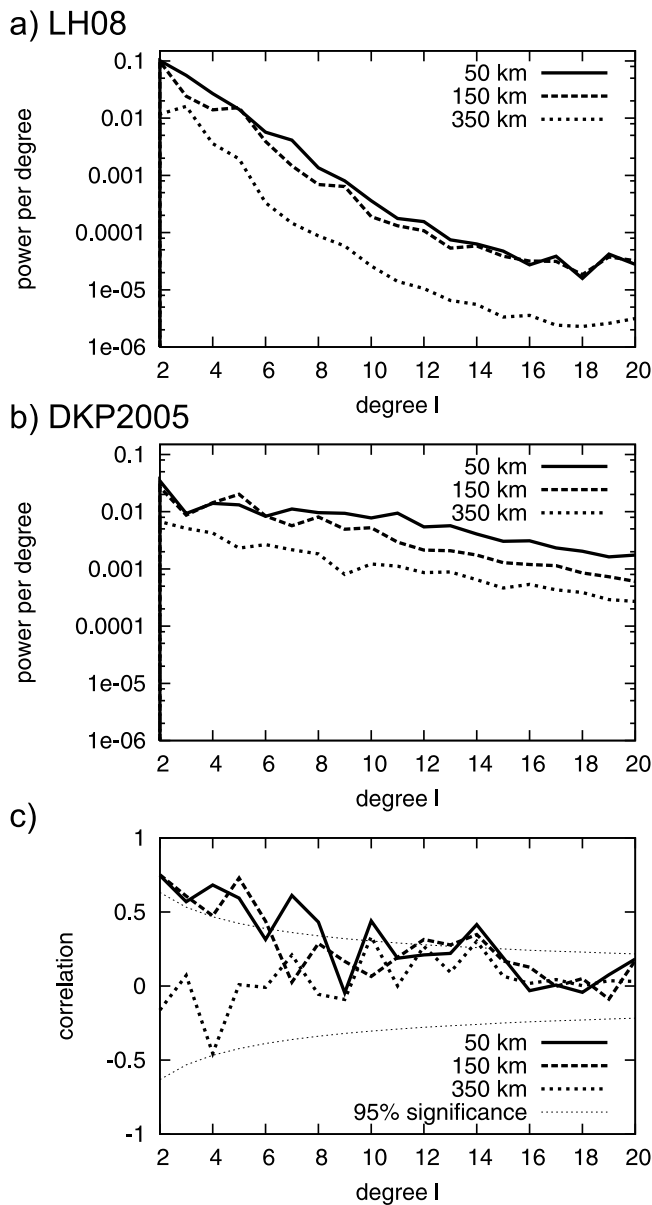
Figure 4. Spatial wavelength-dependent comparison of azimuthal anisotropy (2Ψ anomaly signal for *SV* wave speeds) from the tomographic models by (a) *Lebedev and van der Hilst* [2008] (LH08) and (b) *Debayle et al.* [2005] (DKP2005). Figures 4a and 4b show power per degree and unit area (note log scale) against spherical harmonic degree ℓ at three layer depths as indicated. (c) The linear correlation per degree of azimuthal anisotropy between the two seismological models, along with the 95% significance level based on Student's *t*-test. All metrics are computed using generalized spherical harmonics based on the $A_{c,s}$ terms of equation (3) (for details, see *Becker et al.* [2007b]).

anomaly of 1.2%. To see how much radial change in structure is mapped by these models, Figure 5b shows the total correlation up to $\ell = 20$, r_{20}, between two layers at $z_{1,2} = z \pm 100$ km for the layer at z under consideration. DKP2005 has large change in structure at ~200 km depth [*Debayle et al.*, 2005], whereas LH08 is also vertically very smooth (cf. Figure 2), presumably at this point mainly

reflecting choices as to the effective radial smoothing of the tomographic inversions. The overall match between the models as a function of depth is shown in Figure 5c; it peaks at total correlation values of $r_{20} \sim 0.5$ at ~100 km depth but falls below 95% significance at ~300 km.

[24] These differences in spectral character and the relatively poor match between models reflect current challenges in finding consistent, anisotropic tomography models for the upper mantle and the importance of regularization choices which differ between authors [cf. *Becker et al.*, 2007b, 2008]. To provide another point of comparison, we also compute the correlation of azimuthal anisotropy from each surface wave model with the geodynamic flow modeling approach that was optimized by *Becker et al.* [2008] regarding its match to entirely different, radial anisotropy tomography by *Kustowski et al.* [2008]. The correlation with the geodynamic prediction peaks at ~0.3 for DKP2005, and ~0.5 for LH08. The match between azimuthal anisotropy from LH08 and the geodynamic model is thus overall better

a)

b)

c)
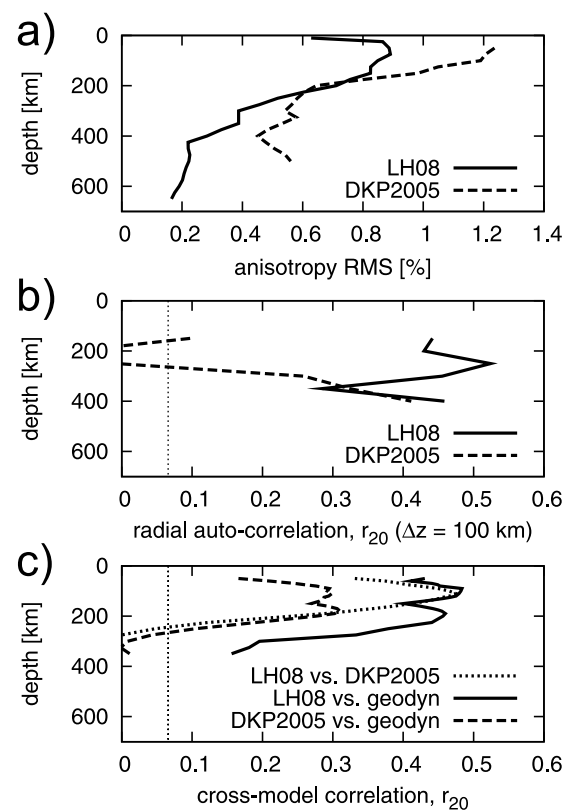
Figure 5. Depth-dependent properties of tomographic models of azimuthal anisotropy. (a) Root mean square (RMS) of the 2Ψ anomalies $((v_{SV1} - v_{SV2})/v_{SV})$ in the models by *Lebedev and van der Hilst* [2008] (LH08) and *Debayle et al.* [2005] (DKP2005) as a function of depth, when both models are expressed in generalized spherical harmonics with maximum degree $L = 20$. (b) Correlation up to $\ell = 20$, r_{20}, between two layers of the same model at $z_{1,2} = z \pm 100$ km, plotted as a function of depth z; 95% significance level shown (see also Figure 2). (c) Cross-model correlation between the two seismological models and of each with the best-fit geodynamic model of *Becker et al.* [2008].
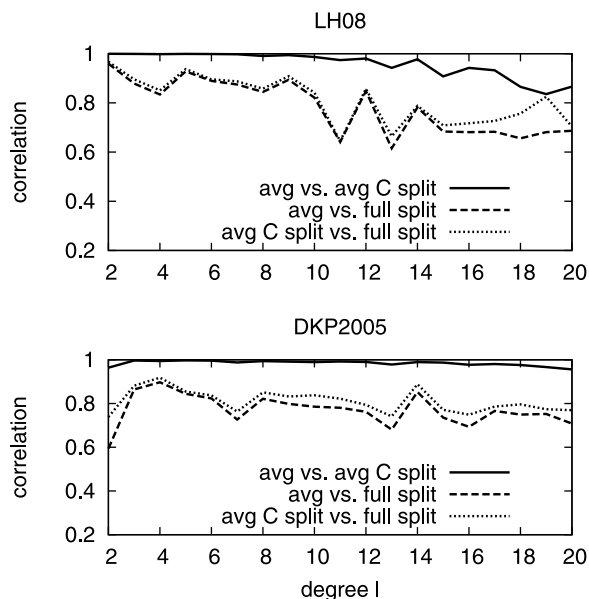
Figure 6. Wavelength-dependent correlation between the predicted splitting ϕ' and $\delta t'$ computed using three different methods as described in section 2 on the basis of tomography by (top) *Lebedev and van der Hilst* [2008] and (bottom) *Debayle et al.* [2005]. Solid line indicates the comparison between *Montagner et al.* [2000] averaging and Christoffel matrix from an averaged tensor approach; dashed line indicates *Montagner et al.* [2000] versus full waveform split; dotted line indicates Christoffel matrix approach from averaged tensor versus full waveform, synthetic splitting.

than the match between the seismological models, confirming that the anisotropy inferred from mantle flow estimates provides a meaningful reference for geodynamic interpretation [*Long and Becker*, 2010].

4. Results

[25] We proceed to describe the results from different predicted splitting methods and when predicted splitting is compared to actual data. If splitting is to be estimated at a certain location, as in the case for the comparison with actual splitting observations, we interpolate the original $A_{c,s}$ values from the tomographic models to that location, assembling a vertical, upper mantle stack of $C(z)$ tensors, and then compute ϕ' and $\delta t'$. Alternatively, if global estimates of statistical properties are required, we construct roughly $2° \times 2°$ gridded representations of ϕ' and $\delta t'$ on regularly spaced sites on the surface of the globe, and extract information from these. Given the smooth nature of LH08, the site-specific values for predicted splitting are very similar to those that can be interpolated from the global representations for LH08. However, as noted by *Wüstefeld et al.* [2009], the relatively more heterogeneous model DKP2005 requires a finer representation. We therefore use global representations for intertomography model comparisons, and geographic site-specific interpolations directly from $A_{c,s}$ of tomography for comparisons with actual splits. We limit all of our geographic analysis to polar-distant latitudes of $\lambda \in [-80°; 80°]$

to ensure that the uncertainty due to the smoothing of the anisotropy terms $A_{c,s}$ in LH08 is not affecting our analysis.

4.1. Shear Wave Splitting From Tomographic Models

[26] We now consider the global statistical deviations between different methods of estimating predicted splitting from tomographic models of azimuthal anisotropy. We first use the $A_{c,s}$ terms of equation (3) within the depth region in which both LH08 and DKP2005 are defined, which ranges from 75 to 410 km. We interpolate the original layers to a consistent, 25 km spaced representation and then compare results from *Montagner et al.* [2000] averaging with the Christoffel matrix from averaged tensors, and the full waveform, synthetic splitting approach described above.

[27] Figure 6 compares results obtained for predicted splitting using a vertically assembled, $C(z)$ models based on
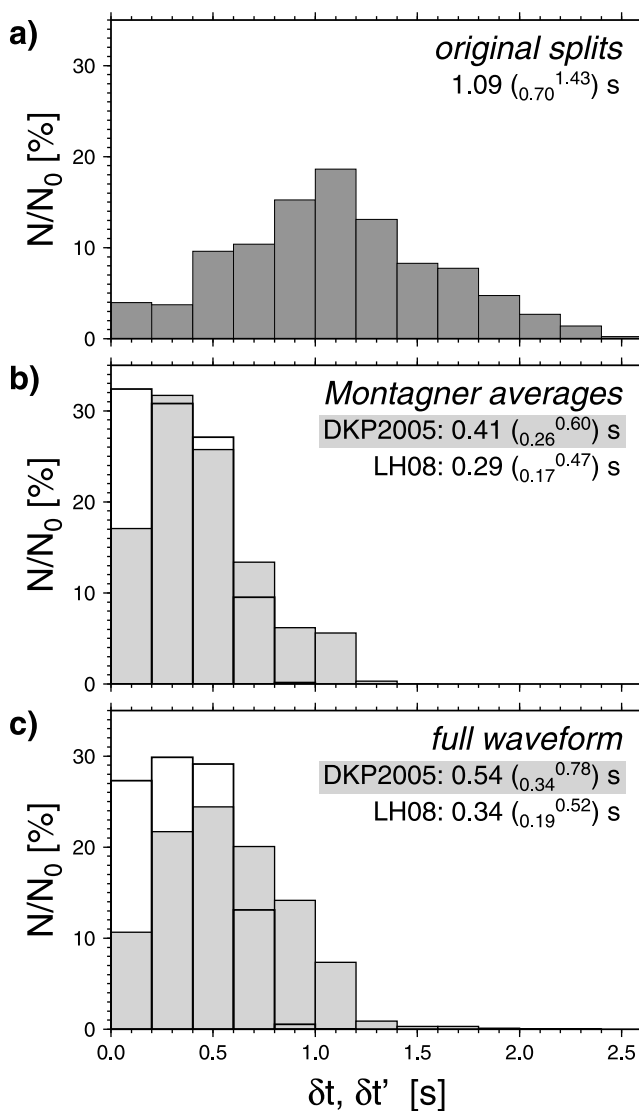
Figure 7. (a) Distribution of delay time in the station-averaged splitting database if predicted from tomography using (b) *Montagner et al.* [2000] averaging and (c) on the basis of full waveform splits. Median values of distribution given along with Q_1 and Q_2 quartiles in parentheses.

a horizontally aligned, hexagonal tensor oriented and scaled based on $A_{c,s}(z)$ terms, when expressed in generalized spherical harmonics up to $L = 20$.

[28] The Christoffel matrix approach for a depth-averaged tensor leads to similar predictions to the *Montagner et al.* [2000] average, particularly at the longest wavelengths, but back-azimuth variations due to effectively dipping symmetry axis lead to slight deviations at shorter scales ($r_{20} \approx 1.00$ and 0.99 for LH08 and DKP2005, respectively). The full waveform results are broadly consistent with the simple averaging, but total correlations are decreased to $r_{20} \approx 0.90$ and 0.78 for the two models, respectively. Using the Christoffel approach gives a slightly better match to full waveform splitting, $r_{20} \approx 0.91$ and 0.82, respectively. The relative agreement between methods is thus better for LH08 than for DKP2005, which is expected given the more heterogeneous representation of Earth structure of the latter model (Figures 2, 4, and 5).

[29] The regional patterns of mismatch are strongly model-dependent and show no clear geographic association besides an indication for larger angular deviations, $\Delta\alpha = \phi - \phi'$, for the ϕ/ϕ' "axes" within continents, and underpredicted δt in young, spreading-center proximal regions when comparing *Montagner et al.* [2000] averages to full waveform splitting.

[30] Expressed in perhaps more intuitive terms, the absolute angular mismatch, $|\Delta\alpha|$ ($|\Delta\alpha| \in [0, 90°]$), between *Montagner et al.* [2000] averaging and the full waveform, synthetic splitting method are $15 \pm 15°$ and $21 \pm 18°$ for LH08 and DKP2005, respectively, with global mean $\pm$ standard deviation indicated. These values reflect large spatial variability in the mismatch, and the means are comparable to, and perhaps a bit larger than, typical splitting measurement uncertainties in ϕ, $\Delta\phi$ (median uncertainty is $\Delta\phi = 15°$ in our compilation). The average and standard deviation of the delay time differences are -0.05 ± 0.08 s and -0.07 ± 0.13 s for LH08 and DKP2005, respectively. The spatial variability of the δt mismatch is therefore ~ 0.1 s, smaller than the typical delay time uncertainty of splits (median uncertainty 0.2 s in our compilation). Delay times themselves from the *Montagner et al.* [2000] method and full waveform splits are correlated at the 0.94 and 0.82 level for LH08 and DKP2005, respectively, based on $L = 20$ expansions. (We only quote linear, Pearson correlation coefficients here, but Spearman rank-order values (see, e.g., *Press et al.* [1993, pp. 636 and 640] for definitions) are generally very similar.)

[31] Table 1 shows correlations and linear regression parameters between different, full waveform, synthetic splitting methods and the *Montagner et al.* [2000] averaging. Results are broadly independent of detailed choices of how anisotropy is represented or how the measurement is made on the waveforms. If longer period filtering is applied (making the measurement more consistent with the assumptions inherent in the work of *Montagner et al.* [2000]), correlations are almost unchanged, but delay times increase. With moderate filtering between 7 and ~ 12 s periods, the waveform methods predict between $\sim 10\%$ and $\sim 40\%$ larger delay times than *Montagner et al.* [2000] averaging when the depth region between 75 and 410 km is considered. The largest changes in correlation in Table 1 are seen when anisotropy is restricted to the perhaps best constrained depth regions between 25 and 250 km. In this case, correlations are improved (and delay times relatively underpredicted by the waveform methods). We will explore the depth dependence in a comparison with actual splitting below.

[32] With the caveat that tomography provides a lower bound for the degree of heterogeneity in the Earth, the simplified method of relating tomography to shear wave splitting is therefore generally valid, even if the assumptions inherent in the derivation of *Montagner et al.* [2000] are not strictly fulfilled by actual splitting measurements [e.g., *Silver and Long*, 2011]. Typical differences in regional delay times are comparable to common uncertainties in the individual measurement and a bit larger for the more heterogeneous tomography of *Debayle et al.* [2005]. This implies that the full waveform, synthetic splitting approach might still be required for reliable estimates in settings with higher complexity.

[33] An advantage of the full waveform method of predicting splitting is that the back-azimuthal variations of ϕ and δt can, at least in theory, be used as additional information [cf. *Becker et al.*, 2006b]. For simplicity, we measure the back-azimuthal dependency of variations in splitting by the standard deviation of ϕ and δt when splits are computed for all possible back-azimuths, here from 0° to 360° in steps of 2°, and call those "complexities" σ_ϕ and $\sigma_{\delta t}$. The global mean values and standard deviations are $\langle \sigma_\phi \rangle \sim 16 \pm 7°$ and $\langle \sigma_{\delta t} \rangle \sim 0.17 \pm 0.1$ s for both LH08 and DKP2005 (median values are close to the mean), using the 75–410 km depth range for reference. The maximum complexities are $\sigma_\phi \sim 50°$ and $\sigma_{\delta t} \sim 1$ s, respectively, indicating that, regionally, such back-azimuth effects might be important when comparing synthetics and real splitting.

[34] If we map this splitting complexity based on the full waveform splits for the two tomographic models considered, the regional variations are, again, not clearly associated with any tectonic or geographic features, and look quite different for the two tomographic models. One exception is $\sigma_{\delta t}$ for LH08 which is larger (~ 0.2 s) for (young) oceanic regions, compared to continental regions (~ 0.11 s). No such relationship exists for synthetics from DKP2005.

[35] Given that we expect splitting complexity, and the deviations between full waveform splitting and *Montagner et al.* [2000] averaging, to be affected by local, depth-variable anisotropy effects such as rotation of Ψ [e.g., *Saltzer et al.*, 2000], it would be desirable to have a simple metric to decide if full waveform treatments are needed. However, on a global scale, we could not easily find such a metric. We tested the total, absolute rotation of Ψ with depth, as well as a similar measure that scaled angular difference with depth by the anisotropy strength for the particular layers. Only the latter measure showed some predictive power, but global correlations with $\sigma_{\delta t}$ and σ_ϕ were low, of order 0.2 for DKP2005, and 0.45 for σ_ϕ and 0.13 for $\sigma_{\delta t}$ for LH08. If we restrict ourselves to the perhaps better constrained depth regions of the tomographic models from 25 to 250 km, the correlations between the scaled measure of rotation and splitting complexity are still only ~ 0.3 for DKP2500 and LH08. This somewhat surprising result implies that the nonlinearity of the splitting measurement may not lend itself well to simplified estimates of splitting complexity.

Table 1. Relationship Between *SKS* Splitting Delay Time Predictions Based on Vectorial Averaging of Azimuthal Anisotropy Tomography and Full Waveform Approaches for the Two Tomographic Models[a]

	LH08 Linear Regression			DKP2005 Linear Regression		
Type of Computation	Correlation	Offset a	Slope b	Correlation	Offset a	Slope b
Reference	0.94	0	1.10	0.82	0	1.17
$T \approx 12.5$ s filtering	0.93	−0.06	1.41	0.84	−0.03	1.33
$T \approx 15$ s filtering	0.81	−0.11	1.86	0.84	−0.05	1.38
Depth-dependent C	0.93	0	1.10	0.82	0	1.18
Depth-dependent C, variable dip	0.93	0	1.05	0.82	0	1.12
Menke and Levin [2003] method	0.94	0	1.23	0.84	0	1.02
Using 25–250 km depths	0.98	0	0.89	0.94	0	0.88

[a]Vectorial averaging of azimuthal anisotropy tomography is from *Montagner et al.* [2000]. Reference method uses scaled, purely hexagonal tensors C at all depths from 75 to 410 km, filtering with central period $T \approx 7$ s, and the *Levin et al.* [1999] method. The best-fit slope, b, is computed from a linear regression (allowing for "errors" in both variables) such that $\delta t'_{\text{waveform}} \approx a + b \, \delta t'_{\text{Montagner}}$.

4.2. Match Between Actual and Predicted Splitting

4.2.1. Delay Times

[36] Figure 7 compares the delay times evaluated at the station-averaged splitting database (with globally uneven distribution as in Figures 1 and 3a) with those predicted from the two tomographic models using the simplified and full waveform approach. (The DKP2005 predictions in Figure 7b replicate *Wüstefeld et al.* [2009] results for a slightly different database; they are consistent.) As expected from the analysis above, the two predicted splitting methods in Figures 7b and 7c give broadly consistent answers. On the basis of the reference depth range of 75–410 km, median delay time predictions are ∼50% of the original splits for DKP2005 and ∼30% for LH08, respectively. This reflects the differences in the azimuthal anisotropy power in the two tomographic models (e.g., Figure 4), and the general tendency of global tomographic models to underpredict actual amplitudes given the necessary regularization choices.

[37] In particular, predicted delay times are shifted toward zero (∼0.4 s) (Figure 7c) compared to the actual splits which cluster at ∼1.1 s (Figure 7a). This shift is due to a reduction in anomaly amplitudes because of the strong lateral and moderate vertical averaging (roughness damping, as in LH08, for example). In some tomographic inversions, norm damping may also contribute, where the assumption is that of a Gaussian distribution of anisotropic anomalies around a zero mean. This may not be appropriate for a description of seismic anisotropy in the upper mantle. Resulting amplitude differences between predicted and actual splitting are less pronounced for regional comparisons of azimuthal anisotropy models [e.g., *Deschamps et al.*, 2008b].

[38] Figures 3c and 3d show the predicted splitting evaluated on the 5° bin-averaged splitting locations for LH08 and DKP2005, respectively, sorted into tectonic regions to test for geographic variations of typical delay times. The slight trend of larger average delay times for oceanic versus continental regions as seen in actual splitting (Figure 3b) is stronger in predicted splitting for both models (as noted by *Wüstefeld et al.* [2009] for DKP2005), and $\delta t'$ is particularly large for the youngest oceanic lithosphere for LH08 (Figure 3c) and for orogenic zones in DKP2005 (Figure 3d).

4.2.2. Fast Polarization Match

[39] If we consider the spherical harmonics representation of our splitting database, the total correlation with the predicted splits (using both ϕ and δt information, as

expressed by $A_{c,s}$ factors, see Appendix A) computed for the full waveform method for LH08 and DKP2005 are $r_{20} \sim 0.35$ and $r_{20} \sim 0.25$, respectively. However, when correlations are computed per degree (as for the model comparison in Figure 4c), only the very longest wavelength terms are above 95% statistical significance ($\ell = 2$ for DKP2005, $\ell = 2,3$ for LH08). This implies that, globally, the match between predicted splitting from tomography and actual splits might only be recovered when the longest wavelengths are considered (cf. Figures 1 and 2).

[40] Figure 2 compares the 2Ψ fast propagation direction of the tomographic models, the predicted splitting and variability, from the full waveform method, and the actual splitting in the 5° degree averaged representation on global maps. These plots highlight the differences in the tomographic models (cf. Figures 4 and 5) with resulting variations both in the predicted splitting, and the back-azimuth variations thereof. From visual inspection (Figure 2), it is apparent that the actual *SKS* splits are matched in some regions, but not in others [cf. *Montagner et al.*, 2000; *Wüstefeld et al.*, 2009] and that there are systematic, large-scale deviations in angle for LH08.

[41] Table 2 lists the median and standard deviations of the absolute, angular misfit between full waveform, synthetic splitting and the station-averaged and 5° averaged representation of actual splits, when computed for different depth ranges and different tomographic models. LH08 leads to overall slightly better predictions of the measured *SKS*

Table 2. Median and Standard Deviation of the Absolute Angular Misfit, |Δα|, Between Full Waveform Synthetic Splitting and Our Station-Averaged *SKS* Compilation for the Complete Database and the 5°-Binned Representation in Figure 2[a]

	Median ± Standard Deviation of |Δα| (deg) Integration Depth Ranges			
Type of Database	75–410 km	25–250 km	10–410 km	25–650 km
	*LH*08			
All splits	33 ± 25	30 ± 25	31 ± 25	37 ± 26
5°-averaged	34 ± 26	32 ± 26	31 ± 26	34 ± 26
	*DKP*2005			
All splits	39 ± 25	38 ± 26	37 ± 25	40 ± 25
5°-averaged	37 ± 25	38 ± 26	38 ± 26	41 ± 27

[a]Random average value is |Δα|$_r$ = 45°. We show results for different tomographic models and depth ranges used for integration.

Table 3. Comparison of Median Absolute Angular Misfit, |$\Delta\alpha$|, Between Predicted and Actual *SKS* Splitting Based on a 5°-Averaged Representation of Our Dataset and an Integration of LH08 in the Depth Range of 25–250 km[a]

Type of Model	Median of Angular Misfit |$\Delta\alpha$| (deg)								
	Global	Oceanic	Continental			Ψ Rotation		σ_ϕ	
			Orogenic	Platforms	Shields	Low	High	Low	High
Montagner et al. [2000] averaging	33	28	36	36	38	24	36	35	36
Full waveform	32	27	30	35	41	24	36	32	35
Full waveform, $\pm\sigma_\phi$	19	14	18	20	22	11	24	29	13

[a]We list median angular misfits for all data locations and when sorted into (1) the tectonic regionalization of *Jordan* [1981] (cf. Figure 3); (2) the smallest and largest 25% of total, depth-integrated, nonamplitude-scaled rotation of the tomographic fast direction, Ψ; and (3) the smallest and largest 25% of estimated back-azimuth variability, σ_ϕ, from full waveform splitting.

splitting, with typical values |$\Delta\alpha$| $\sim$ 33° compared to |$\Delta\alpha$| $\sim$ 38° for DKP2005. These misfits are significantly smaller than the expected random value, |$\Delta\alpha$|$_r$ = 45°. There is a large degree of spatial variability in the mismatch, as seen in the standard deviations for |$\Delta\alpha$| which are $\sim$25°. Moreover, splitting predictions are somewhat improved in their match to tomography if the crustal layers above 75 km are taken into account for LH08, or if the integration is restricted to regions above 250 km (Table 2). This indicates that the shallower layers of LH08 may be better constrained and that crustal anisotropy in LH08 is reflected in the splitting signal. Any such trends with depth, if they exist, are less clear for DKP2005.

[42] Table 3 shows some of the regional and methodological variations of the mismatch between predicted and actual splitting and the 5°-averaged splits (to partially account for the spatial bias inherent in the global splitting dataset, cf. Figures 1–3). We use only the well-constrained 25–250 km depth regions of LH08 for illustration where trends appear clearest. Comparing the global angular misfits, predictions are generally improved for full waveform estimates compared to the simplified, *Montagner et al.* [2000] averaging, but only marginally so.

4.2.3. Back-Azimuth Variations

[43] Some of the mismatch between predicted and actual splitting (which is here based on station averages of individual splits) might arise because of variations in apparent splitting with back-azimuth. We can account for this in an idealized fashion if we take the variability information afforded by the waveform method into account. We use the minimum |$\Delta\alpha$| that can be achieved by allowing ϕ' for each site to vary within the range $\phi' \pm \sigma_\phi$. The global, median misfit can then be reduced to 19° for the full waveform splits. This optimistic scenario |$\Delta\alpha$| is about as good as these comparisons get; 19° angular misfit is comparable or somewhat larger than the best match between geodynamic models and shear wave splitting [e.g., *Becker et al.*, 2006a; *Conrad and Behn*, 2010] and better than the match of geodynamic models to surface wave azimuthal anisotropy [e.g., *Gaboret et al.*, 2003; *Becker et al.*, 2003].

[44] Uneven back-azimuthal coverage may also bias station-averaged splitting parameter estimates in a general way. In the absence of back-azimuth information for most of the splits in the database, we computed global maps of the theoretical back-azimuth coverage that might be expected given natural seismicity and the location where a splitting measurement is made [*Chevrot*, 2000]. Such maps can be constructed, for example, by selecting, for each locale, the

events within the *SKS* splitting typical distance range from 90°−145° with magnitudes larger than 5.8 from the *Engdahl et al.* [1998] catalog between 1988 and 1997, as in the work of *Chevrot* [2000]. We then sum these events into 10° back-azimuthal angle bins and define completeness, *f*, by the number of bins with more than five events, divided by the total number of bins.

[45] To provide an idea of the spatial variability in, and robustness of, such maps, Figure 8 compares the resulting map for completeness with one where we selected all events in the Harvard global CMT database [*Dziewonski et al.*, 2010] up to 2010 for the more restrictive range of 90°−130° instead. When broken into four regions of degree of completeness, neither the maps themselves, nor a combination with the back-azimuth variations from predicted splitting, showed robust trends regarding the misfit between predicted and actual splitting. This does not rule out that back-azimuthal variations, perhaps as predicted from full waveform splitting, could be used to quantitatively explore the origin of the misfit between predicted and real splits, but more information about the actual events associated with each split is needed.

[46] We also tested if the character of the tomographic model could be used to predict average misfit values. Among the integrated rotation metrics considered above for prediction of mismatch between *Montagner et al.* [2000] averaging and full waveform methods, only the simple integration that did not weigh each layer rotation of Ψ by anisotropy strength showed some spatial predictive power. Regions of high overall rotation show larger deviations than those with more coherent anisotropy (Table 3). For the scaled, depth-integrated rotation (which had some, albeit small predictive power for the deviation between simple averaging and waveform splitting), the case is reversed, and the larger integrated rotation sites have a smaller median misfit. If we use the predicted, back-azimuth variability from full waveform splitting, σ_ϕ, to sort regions of misfit, the median |$\Delta\alpha$| is slightly higher in those domains with the highest variability for the full waveform splitting results. (Misfit values for low and high variability are inverted for the optimistic scenario in which we allow $\phi' \pm \sigma_\phi$ to vary to find the minimum misfit, as expected, because larger σ_ϕ allows for larger adjustment.)

4.2.4. Wavelength Dependence and Smoothing

[47] To evaluate the global relationship between predicted and real splitting further, we compute angular misfits and delay time correlations for different, bin-averaged
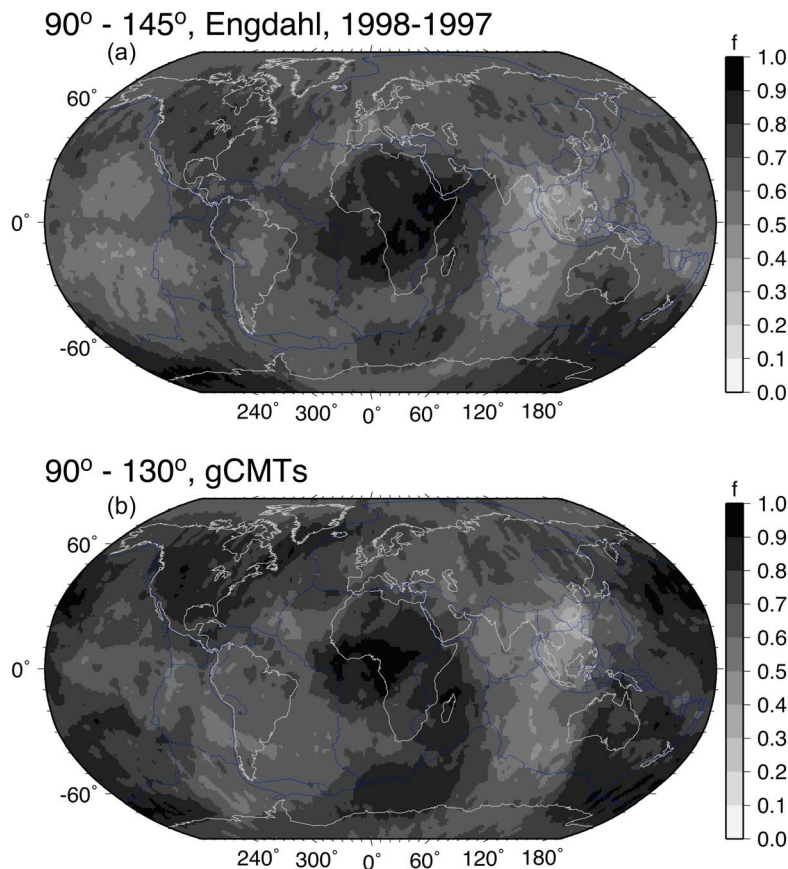
Figure 8. (a) Back-azimuthal completeness for shear wave splitting, *f*, for all events above magnitude 5.8 in the *Engdahl et al.* [1998] catalog from 1988 to 1997 within the distance range of 90°−145° (for comparison with *Chevrot* [2000]). (b) Completeness for all events in the gCMT catalog (www.globalcmt.org) up to 2010 and distance range of 90°−130°.

representations of splitting to ensure we are not biased by the potential artifacts of spatial basis representations.

[48] Figure 9 explores different metrics for the match between predicted and actual splits for our simple, bin-averaging representation of the splitting database, for increasing bin size (or smoothing wavelength). At close-to-original representations of $\gamma = 1°$, both tomographic models predict median, absolute angular misfits, $|\Delta\alpha|$, of ~35° (Figure 9a), but only LH08 shows a positive (small) correlation between $\delta t'$ and δt (Figure 9b). If we increase the averaging γ to ~25° at the equator, the median misfits for both LH08 and DKP2005 are reduced, and delay time correlation for LH08 has a (positive) peak. Consistent with the values shown in Table 3, the restriction to the depths between 25 and 250 km (dotted lines) leads to a better match of splitting for both tomographic models.

[49] While we find the delay time difference and angular misfit instructive, one can also consider the coherence function

$$C(\alpha) = \frac{\sum_{i=1}^{M} \sin^2\Theta_i \, \delta t_i \delta t'_i \exp\left(-\left(\phi_i - \phi'_i + \alpha\right)^2 / \left(2D_c^2\right)\right)}{\sum_{i=1}^{M} \sin^2\Theta_i \, (\delta t_i)^2 \sum_{i=1}^{M} \sin^2\Theta_i \, (\delta t'_i)^2}, \quad (5)$$

due to *Griot et al.* [1998] and used by *Wüstefeld et al.* [2009]. Here, $C(\alpha)$ is expressed as a summation for

$i = 1\ldots M$ of pairs of point data, provided at colatitudes Θ_i, as used in comparing our splitting database (entries ϕ_i and δt_i) with synthetic splitting (ϕ'_i and $\delta t'_i$) from the tomographic models, and D_c is a constant correlation factor [cf. *Wüstefeld et al.*, 2009]. The coherence can be used for comparative purposes between studies, and $C(\alpha)$ also allows detection of a systematic bias in orientations. We show the maximum of the coherence, C_{max}, using $D_c = 20°$ in Figure 9, and the better match for LH08 rather than DKP2005 as seen in the misfit values of Table 3 is reflected in respectively larger maximum coherence. The corresponding C_{max} values are shown in Figure 9c for different averaging lengths, γ, for the actual shear wave splitting. By comparison of the wavelength dependence of C_{max}, it is clear that both a drop in mean angular misfit (Figure 9a) and an increase in delay time correlation (Figure 9b) are the cause of the dramatic increase of C_{max} for LH08 at larger averaging wavelengths. Maximum coherence for DKP2005 remains fairly flat, mainly because of the poor correlation of predicted and actual delay times.

[50] Given that the C_{max} values in Figure 9c may well be found at α offsets from zero lag, we show the lag dependence of $C(\alpha)$ in Figure 10 for selected averaging bin sizes of $\gamma = 1°$, 10°, and 30°. There is indeed a significant bias in LH08 toward a consistent misalignment of $\alpha \sim -30°$ for the shorter averaging lengths. Excluding North American
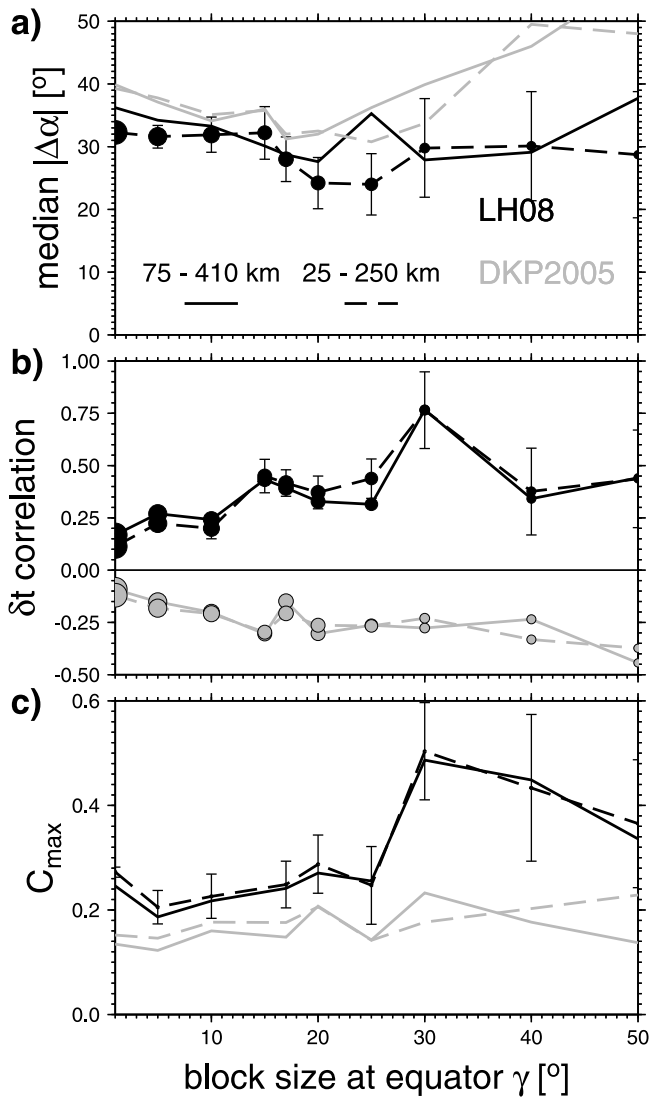
Figure 9. Misfit between predicted and actual splitting when expressed as (a) the median, absolute angular deviation between ϕ and ϕ', (b) the delay time correlation between δt and $\delta t'$, and the maximum coherence, C_{max} (for any lag, α), for $D_c = 20°$ (see equation (5)). All misfit values are shown as a function of bin size, γ, of the averaged splitting; gray shades indicate different tomographic models. Solid lines are for the default depth range of 75–410 km, dashed for 25–250 km (cf. Table 3). Circle symbol size in Figures 9a and 9b scales with the $\log_{10}$ of the number of sites, N, used for analysis; N decreases from 2717 for $\gamma = 1°$ to $N = 16$ for $\gamma = 50°$. Error bars (same for all tomographic models, but only shown for shallow, LH08 curves for simplicity) indicate the standard deviation around the mean for 250, random medium Monte Carlo simulations.

splits from the full database and recomputing $C(\alpha)$ explains most of this shift toward negative α, though the culled dataset still leads to C_{max} at $\alpha \sim -20°$ lag. This highlights the spatially variable character of the match between predicted and actual splitting (Figure 2), which was discussed in a regional $C(\alpha)$ analysis for DKP2005 by *Wüstefeld et al.* [2009]. However, once larger averaging γ is applied,

coherence is increased for LH08, and C_{max} is found at roughly zero lag for $\gamma = 30°$ (Figures 10 and A1).

[51] Eschewing further statistical geographic analysis, but rather considering the match to actual splits when evaluated by geologically distinct regions, the intermethod differences are somewhat larger, and oceanic regions are better predicted than continents (Table 3). Within continents, the geologically young regions are matched better than older ones, with up to 10° difference in median $|\Delta\alpha|$ between orogenic zones and shields for the full waveform approach. This is consistent with the notion of recent asthenospheric flow leading to a simpler connection between convective anisotropy at depth compared to older domains with complex, frozen-in structure as seen by splitting [cf. *Becker et al.*, 2007a; *Wüstefeld et al.*, 2009].

5. Discussion

[52] It is difficult to estimate the true amplitude and, especially, the scale of expected shear wave splitting heterogeneity from global models of seismic anisotropy. Yet, if the difference in lateral resolution of the two types of data is taken into account and treated quantitatively, the predicted and observed splitting parameters display significant agreement.

[53] We find that the global distribution of azimuthal anisotropy is still represented very differently in the most up-to-date tomographic models. Different data and inversion choices lead to different representations of the Earth, as was discussed earlier by *Becker et al.* [2007b] for Rayleigh wave phase-velocity maps. Generally, global models of seismic anisotropy are very smooth due to the unevenness of the azimuthal coverage given the available broadband seismic data. In regions that are sampled relatively poorly, only long-wavelength structure can be resolved accurately, which typically necessitates that the entire model is smoothed strongly. Accumulation of seismic data from new stations installed in the last few years, particularly in the oceans, can be expected to result in a stronger agreement between
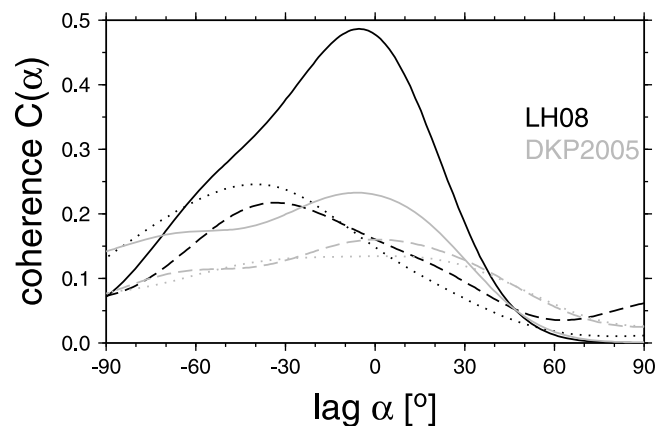
Figure 10. Coherence between predicted (full waveform, depth range of 75–410 km) and actual splitting for $D_c = 20°$ and spatial averaging of the splitting database, where solid line indicates bin width $\gamma = 30°$; dashed line indicates $\gamma = 10°$; and dotted line indicates $\gamma = 1°$ (cf. Figure 9c). Black is for LH08 and gray is for DKP2005.

anisotropic tomography models of a new generation, at least at longer wavelengths, as has been seen for models of isotropic global structure [e.g., *Becker and Boschi*, 2002].

[54] Our results indicate that *SKS*-splitting delay times are severely underpredicted by both tomographic models considered (too small compared to the actual splits by $\sim$ half). One explanation for this discrepancy is that anisotropy as measured by *SKS* splitting might be accumulated in deeper mantle regions such as the transition zone [e.g., *Trampert and van Heijst*, 2002], not (well) covered by the uppermantle tomography models we tested here. However, we consider it unlikely that this is a large effect globally [*Niu and Perez*, 2004]. In some subduction zones, for example, it has been shown that the uppermost mantle dominates the *SKS* splitting signal [e.g., *Fischer and Wiens*, 1996], although some studies have identified a contribution to *SK*(*K*)*S* splitting from lower mantle anisotropy in localized regions [e.g., *Niu and Perez*, 2004; *Wang and Wen*, 2007; *Long*, 2009]. Dominance of uppermost mantle anisotropy for splitting is consistent with the finding that most seismically mapped azimuthal or radial anisotropy resides in the asthenospheric regions above ~300 km, where formation of LPO anisotropy for olivine in the dislocation-creep regime can be quantitatively linked to anisotropy [*Podolefsky et al.*, 2004; *Becker*, 2006; *Becker et al.*, 2008; *Behn et al.*, 2009].

[55] Assuming that the global shear wave splitting data set mainly reflects upper mantle anisotropy, the mismatch between predicted and actual splitting delay time amplitudes may partially be caused by methodological issues specific to the splitting measurements. *Monteillier and Chevrot* [2010] discuss, for example, how the *Silver and Chan* [1988] method may lead to a bias toward larger delay times in the presence of noise. Given that this method is widely used, our compilation of splitting observations may thus reflect such a bias compared to the synthetic splits. However, we do not consider such methodological problems to be the main source of the discrepancy but rather think that the delay time mismatch gives some guidance as to how much azimuthal anisotropy amplitudes might be underpredicted in global tomographic models. Such a reduction in amplitude naturally results from the necessary regularization of inversions for isotropic and anisotropic structure but also choices as to the representation of Earth structure that might lead to undue smoothing. Smoothness of tomography will also reduce the predicted variations in synthetic splitting fast polarization and delay times as a function of back-azimuth that are seen when adjacent layers have different anisotropy orientations [e.g., *Silver and Savage*, 1994; *Chevrot et al.*, 2004], and such effects may in turn bias actual splitting databases toward larger delay time values.

[56] While computationally expensive, nonlinear approaches to seismic anisotropy tomography may be required to push such analysis further [cf. *Chevrot and Monteiller*, 2009], particularly if regional, high-resolution studies provide a more finely resolved representation of Earth structure. However, delay times between predicted and actual splitting show positive correlation for one of the tomographic models, and it is encouraging that the correlation is seen for the smoother (arguably, more conservative) of the models.

[57] The simple averaging approach that we applied to the original splitting dataset to achieve a good match between LH08 and splitting at averaging lengths of $\gamma \sim 25°$ is inconsistent with findings of strong variations of splits on the shortest, Fresnel-zone length (e.g., discussions by *Fouch and Rondenay* [2006] and *Chevrot and Monteiller* [2009]). Yet, it seems to capture the longest wavelength signal represented in the tomographic model. This provides some confidence in the overall consistency of seismic anisotropy mapping efforts at the longest wavelengths.

[58] Global models, therefore, resolve large-scale patterns of azimuthal anisotropy associated, for example, with asthenospheric flow beneath oceanic plates. However, regional anisotropic tomography using data from dense broadband arrays is needed to provide more detailed information on the radial and lateral distribution of anisotropy. In this way, issues such as coupling between lithospheric deformation and asthenopsheric flow beneath tectonically complex areas can be addressed more fully.

6. Conclusions

[59] Global tomographic models of azimuthal anisotropy provide guidance as to the lower bound of expected complexity in seismic anisotropy. For these models, simplified averaging approaches of computing predicted shear wave splitting are generally valid. Full waveform methods need not be applied to predict shear wave splitting from smooth tomographic models.

[60] Full waveform approaches yield estimates of the back-azimuth variation of splitting, however, and accounting for such effects leads to dramatic drops in the median misfit between predicted and actual splitting. Consideration of actual patterns of back-azimuthal variations (observed and predicted) at individual stations may reconcile many of the remaining discrepancies.

[61] Shear wave splitting predicted from smooth tomographic models is consistent with long-wavelength representations of measured shear wave splitting, on global scales. For continents in particular, this implies that their lithosphere's heterogeneity, due to its geological assembly, is reflected in complex anisotropic structure, but simple, long-wavelength smoothed representations have a deterministic asymptote with geodynamic meaning.

Appendix A: Fitting Generalized Spherical Harmonics to *SKS* Splitting Measurements

[62] The azimuths and delay times as seen in global splitting databases display large variations on short spatial scales and are very unevenly distributed globally (Figure 1). However, long-wavelength averaging of splits leads to a significant improvement in the match between azimuthal anisotropy from *SKS* and surface wave tomography (Figure 9). This motivates our exploration of fitting global, generalized spherical harmonics (GSH) [e.g., *Dahlen and Tromp*, 1998, Appendix C] with maximum degree $L = 20$ as basis functions to the *SKS* database (for details, see *Boschi and Woodhouse* [2006] and *Becker et al.* [2007b]).

[63] Assume that the M station-averaged splits at locations $\mathbf{x}^i$ ($i = 1 \ldots M$) are expressed as a $2M$ dimensional vector holding M pairs of equivalent $A_{c,s}$ parameters, $\mathbf{A} = \{A_c^i, A_s^i\}$.
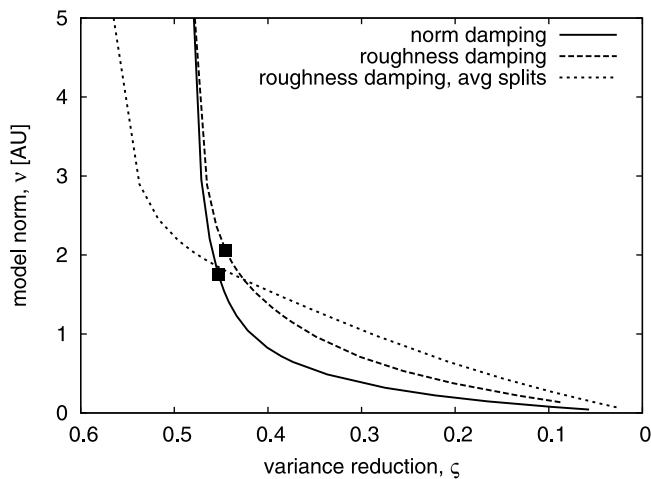
Figure A1. Trade-off curves for damped, least-squares (equation (A1)) fitting GSH basis functions to our global, station-averaged splitting database (as in Figure 1), expressed as model norm, ν (equation (A2)), as a function of variance reduction, ζ (equation (A3)), for norm (R_n) and roughness (R_r) damping with $\omega = 50$ values indicated by squares. Plot also shows a roughness damping trade-off curve for a $1° \times 1°$ averaged representation of the splitting database (see section 3.1).

We then solve a regularized, least-squares inverse problem of type

$$\begin{pmatrix} \mathsf{Y} \\ \mathsf{R} \end{pmatrix} \cdot \mathbf{p} = \begin{pmatrix} \mathbf{A} \\ 0 \end{pmatrix}, \tag{A1}$$

for $\mathbf{p}$, where the $2M \times N$ matrix Y holds the real and imaginary GSH components at the M data locations, $\mathbf{p}$ holds the $N = (2L + 6)(L - 1)$ GSH coefficients for degrees $\ell \in [2; L]$ [see *Becker et al.*, 2007b, equations (8)–(10)], 0 is a N dimensional null vector, and R ($N \times N$) is a damping matrix. For norm damping, we use $\mathsf{R}_n = \omega \, \mathsf{I}$ where I is the identity matrix and ω a damping factor; for wavelength-dependent, "roughness" damping, we use $\mathsf{R}_r = \omega \, \frac{\ell(\ell+1)}{L/2(L/2+1)} \mathsf{I}$ [cf. *Trampert and Woodhouse*, 2003].

[64] To find an adequate representation of the actual splits, we conducted a standard trade-off analysis, evaluating model complexity, expressed by the L_2 norm of $\mathbf{p}$,

$$\nu = \|\mathbf{p}\|, \tag{A2}$$

against misfit, expressed as variance reduction,

$$\zeta = 1 - \|\mathsf{Y} \cdot \mathbf{p} - \mathbf{A}\|/\|\mathbf{A}\|, \tag{A3}$$

using various damping, ω, values. Figure A1 shows the results for norm and roughness damping of the station-averaged splitting dataset.

[65] Both approaches yield typical and consistent "L curves," indicating that a choice of $\omega \sim 50$ (as indicated by the box symbols) yields an appropriate compromise between representing the actual data and arriving at a smooth model. For the analysis in the main text (including Figure 1), we therefore chose $\omega = 50$ and roughness damping to represent

SKS splits in spherical harmonics. That said, the variance reductions that can be achieved are relatively small ($\zeta \sim 45\%$), meaning that aspects of the heterogeneous nature of azimuthal anisotropy from *SKS* splits, expectedly, cannot be captured by our $L = 20$ GSH fit. However, once a $1° \times 1°$ averaging of the splitting database is performed, best ζ values are increased significantly.

References

Ando, M., Y. Ishikawa, and F. Yamasaki (1983), Shear-wave polarization anisotropy in the upper mantle beneath Honshu, Japan, *J. Geophys. Res.*, *88*(B7), 5850–5864.

Babuška, V., and M. Cara (1991), *Seismic Anisotropy in the Earth*, Kluwer Acad., Dordrecht, Netherlands.

Becker, T. W. (2006), On the effect of temperature and strain-rate dependent viscosity on global mantle flow, net rotation, and plate-driving forces, *Geophys. J. Int.*, *167*, 943–957.

Becker, T. W., and L. Boschi (2002), A comparison of tomographic and geodynamic mantle models, *Geochem. Geophys. Geosyst.*, *3*(1), 1003, doi:10.1029/2001GC000168.

Becker, T. W., J. B. Kellogg, G. Ekström, and R. J. O'Connell (2003), Comparison of azimuthal seismic anisotropy from surface waves and finite-strain from global mantle-circulation models, *Geophys. J. Int.*, *155*, 696–714.

Becker, T. W., S. Chevrot, V. Schulte-Pelkum, and D. K. Blackman (2006a), Statistical properties of seismic anisotropy predicted by upper mantle geodynamic models, *J. Geophys. Res.*, *111*, B08309, doi:10.1029/2005JB004095.

Becker, T. W., V. Schulte-Pelkum, D. K. Blackman, J. B. Kellogg, and R. J. O'Connell (2006b), Mantle flow under the western United States from shear wave splitting, *Earth Planet. Sci. Lett.*, *247*, 235–251.

Becker, T. W., J. T. Browaeys, and T. H. Jordan (2007a), Stochastic analysis of shear wave splitting length scales, *Earth Planet. Sci. Lett.*, *259*, 29–36.

Becker, T. W., G. Ekström, L. Boschi, and J. W. Woodhouse (2007b), Length scales, patterns, and origin of azimuthal seismic anisotropy in the upper mantle as mapped by Rayleigh waves, *Geophys. J. Int.*, *171*, 451–462.

Becker, T. W., B. Kustowski, and G. Ekström (2008), Radial seismic anisotropy as a constraint for upper mantle rheology, *Earth Planet. Sci. Lett.*, *267*, 213–237.

Behn, M. D., G. Hirth, and J. R. Elsenbeck II (2009), Implications of grain size evolution on the seismic structure of the oceanic upper mantle, *Earth Planet. Sci. Lett.*, *282*, 178–189.

Bird, P. (2003), An updated digital model of plate boundaries, *Geochem. Geophys. Geosyst.*, *4*(3), 1027, doi:10.1029/2001GC000252.

Booth, D. C., and S. Crampin (1985), The anisotropic reflectivity technique: Theory, *Geophys. J. R. Astron. Soc.*, *72*, 31–45.

Boschi, L., and J. H. Woodhouse (2006), Surface wave ray tracing and azimuthal anisotropy: A generalized spherical harmonic approach, *Geophys. J. Int.*, *164*, 569–578.

Bowman, J. R., and M. A. Ando (1987), Shear-wave splitting in the upper-mantle wedge above the Tonga subduction zone, *Geophys. J. R. Astron. Soc.*, *88*, 24–41.

Browaeys, J., and S. Chevrot (2004), Decomposition of the elastic tensor and geophysical applications, *Geophys. J. Int.*, *159*, 667–678.

Chapman, C. H., and P. M. Shearer (1989), Ray tracing in azimuthally anisotropic media—II. Quasi-shear wave coupling, *Geophys. J. Int.*, *96*, 65–83.

Chevrot, S. (2000), Multichannel analysis of shear wave splitting, *J. Geophys. Res.*, *105*(B9), 21,579–21,590, doi:10.1029/2000JB900199.

Chevrot, S., and V. Monteiller (2009), Principles of vectorial tomography—The effects of model parametrization and regularization in tomographic imaging of seismic anisotropy, *Geophys. J. Int.*, *179*, 1726–1736.

Chevrot, S., N. Favier, and D. Komatitsch (2004), Shear wave splitting in three-dimensional anisotropic media, *Geophys. J. Int.*, *159*, 711–720.

Conrad, C. P., and M. Behn (2010), Constraints on lithosphere net rotation and asthenospheric viscosity from global mantle flow models and seismic anisotropy, *Geochem. Geophys. Geosyst.*, *11*, Q05W05, doi:10.1029/2009GC002970.

Dahlen, F. A., and J. Tromp (1998), *Theoretical Global Seismology*, Princeton Univ. Press, Princeton, N. J.

Debayle, E., B. L. N. Kennett, and K. Priestley (2005), Global azimuthal seismic anisotropy and the unique plate-motion deformation of Australia, *Nature*, *433*, 509–512.

Deschamps, F., S. Lebedev, T. Meier, and J. Trampert (2008a), Azimuthal anisotropy of Rayleigh-wave phase velocities in the east-central United States, *Geophys. J. Int.*, *173*, 827–843.

Deschamps, F., S. Lebedev, T. Meier, and J. Trampert (2008b), Stratified seismic anisotropy reveals past and present deformation beneath the East-central United States, *Earth Planet. Sci. Lett.*, *274*, 489–498.

Dziewonski, A. M., G. Ekström, and M. Nettles (2010), The Global Centroid-Moment-Tensor (CMT) Project, Lamont-Doherty Earth Obs., Palisades, N. Y. [Available at www.globalcmt.org].

Endrun, B., S. Lebedev, T. Meier, C. Tirel, and W. Friederich (2011), Complex layered deformation within the Aegean crust and mantle revealed by seismic anisotropy, *Nat. Geosci.*, *4*, 203–207.

Engdahl, E. R., R. D. van der Hilst, and R. Buland (1998), Global teleseismic earthquake relocation with improved travel times and procedures for depth determination, *Bull. Seismol. Soc. Am.*, *88*, 722–743.

Fischer, K. M., and D. A. Wiens (1996), The depth distribution of mantle anisotropy beneath the Tonga subduction zone, *Earth Planet. Sci. Lett.*, *142*, 253–260.

Fouch, M. (2003), Upper-mantle anisotropy database, School of Earth and Space Explor., Ariz. State Univ., Tempe, Ariz. [Available at http://geophysics.asu.edu/anisotropy/upper/].

Fouch, M. J., and S. Rondenay (2006), Seismic anisotropy beneath stable continental interiors, *Phys. Earth Planet. Inter.*, *158*, 292–320.

Fukao, Y. (1984), Evidence from core-reflected shear waves for anisotropy in the Earth's mantle, *Nature*, *371*, 149–151.

Gaboret, C., A. M. Forte, and J.-P. Montagner (2003), The unique dynamics of the Pacific Hemisphere mantle and its signature on seismic anisotropy, *Earth Planet. Sci. Lett.*, *208*, 219–233.

Griot, D.-A., J.-P. Montagner, and P. Tapponnier (1998), Confrontation of mantle seismic anisotropy with two extreme models of strain, in central Asia, *Geophys. Res. Lett.*, *25*(9), 1447–1450, doi:10.1029/98GL00991.

Hall, C. E., K. M. Fischer, E. M. Parmentier, and D. K. Blackman (2000), The influence of plate motions on three-dimensional back arc mantle flow and shear wave splitting, *J. Geophys. Res.*, *105*(B12), 28,009–28,033, doi:10.1029/2000JB900297.

Jordan, T. H. (1981), Global tectonic regionalization for seismological data analysis, *Bull. Seismol. Soc. Am.*, *71*, 1131–1141.

Karato, S.-I. (1992), On the Lehmann discontinuity, *Geophys. Res. Lett.*, *19*(22), 2255–2258, doi:10.1029/92GL02603.

Kennett, B. L. N. (1983), *Seismic Wave Propagation in Stratified Media*, Cambridge Univ. Press, New York.

Kustowski, B., G. Ekström, and A. M. Dziewoński (2008), Anisotropic shear-wave velocity structure of the Earth's mantle: A global model, *J. Geophys. Res.*, *113*, B06306, doi:10.1029/2007JB005169.

Laske, G., and G. Masters (1998), Surface-wave polarization data and global anisotropic structure, *Geophys. J. Int.*, *132*, 508–520.

Lebedev, S., and R. D. van der Hilst (2008), Global upper-mantle tomography with the automated multimode inversion of surface and S-wave forms, *Geophys. J. Int.*, *173*, 505–518.

Levin, V., W. Menke, and J. Park (1999), Shear wave splitting in the Appalachians and the Urals: A case for multilayered anisotropy, *J. Geophys. Res.*, *104*(B8), 17,975–17,993, doi:10.1029/1999JB900168.

Levin, V., D. Okaya, and J. Park (2007), Shear wave birefringence in wedge-shaped anisotropic regions, *Geophys. J. Int.*, *168*, 275–286.

Lin, F., M. H. Ritzwoller, Y. Yang, M. P. Moschetti, and M. J. Fouch (2011), Complex and variable crustal and uppermost mantle seismic anisotropy in the western United States, *Nat. Geosci.*, *4*, 55–61.

Long, M. D. (2009), Complex anisotropy in D″ beneath the eastern Pacific from SKS-SKKS splitting discrepancies, *Earth Planet. Sci. Lett.*, *283*, 181–189.

Long, M. D., and T. W. Becker (2010), Mantle dynamics and seismic anisotropy, *Earth Planet. Sci. Lett.*, *297*, 341–354.

Long, M. D., and R. D. van der Hilst (2005), Estimating shear-wave splitting parameters from broadband recordings in Japan: A comparison of three methods, *Bull. Seismol. Soc. Am.*, *95*, 1346–1358.

Marone, F., and F. Romanowicz (2007), The depth distribution of azimuthal anisotropy in the continental upper mantle, *Nature*, *447*, 198–201.

Menke, W., and V. Levin (2003), The cross-convolution method for interpreting SKS splitting observations, with application to one- and two-layer anisotropic Earth models, *Geophys. J. Int.*, *154*, 379–392.

Montagner, J. P., and D. L. Anderson (1989), Petrological constraints on seismic anisotropy, *Phys. Earth Planet. Inter.*, *54*, 82–105.

Montagner, J. P., and H. C. Nataf (1988), Vectorial tomography—I. Theory, *Geophys. J. Int.*, *94*, 295–307.

Montagner, J.-P., and T. Tanimoto (1991), Global upper mantle tomography of seismic velocities and anisotropies, *J. Geophys. Res.*, *96*, 20,337–20,351.

Montagner, J.-P., D.-A. Griot-Pommera, and J. Lavé (2000), How to relate body wave and surface wave anisotropy?, *J. Geophys. Res.*, *105*(B8), 19,015–19,027, doi:10.1029/2000JB900015.

Monteiller, V., and S. Chevrot (2010), How to make robust splitting measurements for single-station analysis and three-dimensional imaging of seismic anisotropy, *Geophys. J. Int.*, *182*, 311–328.

Nataf, H.-C., I. Nakanishi, and D. L. Anderson (1984), Anisotropy and shear-velocity heterogeneities in the upper mantle, *Geophys. Res. Lett.*, *11*(2), 109–112, doi:10.1029/GL011i002p00109.

Nicolas, A., and N. I. Christensen (1987), Formation of anisotropy in upper mantle peridotites: A review, in *Composition, Structure and Dynamics of the Lithosphere-Asthenosphere System*, Geodyn. Ser., vol. 16, edited by K. Fuchs and C. Froidevaux, pp. 111–123, AGU, Washington, D. C., doi:10.1029/GD016p0111.

Niu, F., and A. M. Perez (2004), Seismic anisotropy in the lower mantle: A comparison of waveform splitting of SKS and SKKS, *Geophys. Res. Lett.*, *31*, L24612, doi:10.1029/2004GL021196.

Panning, M., and G. Nolet (2008), Surface wave tomography for azimuthal anisotropy in a strongly reduced parameter space, *Geophys. J. Int.*, *174*, 629–648.

Panning, M., and B. Romanowicz (2006), A three-dimensional radially anisotropic model of shear velocity in the whole mantle, *Geophys. J. Int.*, *167*, 361–379.

Pedersen, H. A., M. Bruneton, V. Maupin, and SVEKALAPKO Seismic Tomography Working Group (2006), Lithospheric and sublithospheric anisotropy beneath the Baltic shield from surface-wave array analysis, *Earth Planet. Sci. Lett.*, *244*, 590–605.

Plomerová, J., D. Kouba, and V. Babuška (2002), Mapping the lithosphere-asthenosphere boundary through changes in surface-wave anisotropy, *Tectonophysics*, *58*, 175–185.

Podolefsky, N. S., S. Zhong, and A. K. McNamara (2004), The anisotropic and rheological structure of the oceanic upper mantle from a simple model of plate shear, *Geophys. J. Int.*, *158*, 287–296.

Press, W. H., S. A. Teukolsky, W. T. Vetterling, and B. P. Flannery (1993), *Numerical Recipes in C: The Art of Scientific Computing*, 2nd ed., Cambridge Univ. Press, Cambridge, U. K.

Rümpker, G., and P. G. Silver (1998), Apparent shear-wave splitting parameters in the presence of vertically varying anisotropy, *Geophys. J. Int.*, *135*, 790–800.

Rümpker, G., A. Tommasi, and J.-M. Kendall (1999), Numerical simulations of depth-dependent anisotropy and frequency-dependent wave propagation effects, *J. Geophys. Res.*, *104*(B10), 23,141–23,154, doi:10.1029/1999JB900203.

Saltzer, R. L., J. B. Gaherty, and T. H. Jordan (2000), How are vertical shear wave splitting measurements affected by variations in the orientation of azimuthal anisotropy with depth?, *Geophys. J. Int.*, *141*, 374–390.

Savage, M., and P. G. Silver (1993), Mantle deformation and tectonics: Constraints from seismic anisotropy in the western United States, *Phys. Earth Planet. Inter.*, *78*, 207–227.

Schulte-Pelkum, V., and D. K. Blackman (2003), A synthesis of seismic P and S anisotropy, *Geophys. J. Int.*, *154*, 166–178.

Silver, P. G. (1996), Seismic anisotropy beneath the continents: Probing the depths of geology, *Annu. Rev. Earth Planet. Sci.*, *24*, 385–432.

Silver, P. G., and H. H. Chan (1988), Implications for continental structure and evolution from seismic anisotropy, *Nature*, *335*, 34–39.

Silver, P. G., and M. D. Long (2011), The non-commutivity of shear wave splitting operators at low frequencies and implications for anisotropy tomography, *Geophys. J. Int.*, *184*, 1415–1427.

Silver, P. G., and M. K. Savage (1994), The interpretation of shear wave splitting parameters in the presence of two anisotropic layers, *Geophys. J. Int.*, *119*, 949–963.

Tanimoto, T., and D. L. Anderson (1985), Lateral heterogeneity and azimuthal anisotropy of the upper mantle: Love and Rayleigh waves 100–250 s, *J. Geophys. Res.*, *90*(B2), 1842–1858, doi:10.1029/JB090iB02p01842.

Trampert, J., and H. J. van Heijst (2002), Global azimuthal anisotropy in the transition zone, *Science*, *296*, 1297–1299.

Trampert, J., and J. H. Woodhouse (2003), Global anisotropic phase velocity maps for fundamental mode surface waves between 40 and 150 s, *Geophys. J. Int.*, *154*, 154–165.

Vinnik, L., G. L. Kosarev, and L. I. Makeyeva (1984), Anisotropy of the lithosphere from the observations of *SKS* and *SKKS* phases, *Proc. Acad. Sci. USSR*, *278*, 1335–1339.

Vinnik, L. P., L. I. Makeyeva, A. Milev, and Y. Usenko (1992), Global patterns of azimuthal anisotropy and deformation in the continental mantle, *Geophys. J. Int.*, *111*, 433–447.

Wang, Y., and L. Wen (2007), Complex seismic anisotropy at the border of a very low velocity province at the base of the Earth's mantle, *J. Geophys. Res.*, *112*, B09305, doi:10.1029/2006JB004719.

Wessel, P., and W. H. F. Smith (1998), New, improved version of generic mapping tools released, *Eos Trans. AGU*, *79*(47), 579, doi:10.1029/98EO00426.

Wüstefeld, A., and G. Bokelmann (2007), Null detection in shear-wave splitting measurements, *Bull. Seismol. Soc. Am.*, *97*, 1204–1211.

Wüstefeld, A., G. H. R. Bokelmann, G. Barruol, and J. P. Montagner (2009), Identifying global seismic anisotropy patterns by correlating shear-wave splitting and surface-wave data, *Phys. Earth Planet. Inter.*, *176*, 198–212. [Available at http://www.gm.univ-montp2.fr/splitting/DB/.]

Yuan, H., and B. Romanowicz (2010), Lithospheric layering in the North American continent, *Nature*, *466*, 1063–1069.

T. W. Becker, Department of Earth Sciences, University of Southern California, 3651 Trousdale Pkwy., Los Angeles, CA 90089, USA. (twb@usc.edu)

S. Lebedev, Dublin Institute for Advanced Study, 10 Burlington Road, Dublin 4, Ireland.

M. D. Long, Department of Geology and Geophysics, Yale University, PO Box 208109, New Haven, CT 06520, USA.